Evaluating the Roles of Electrolyte Components on the Passivation of Silicon Anodes

Thomas F. Malkowski[a]*, Zhenzhen Yang[b], Robert L. Sacci[a], Stephen E. Trask[b], Marco-Tulio F. Rodrigues[b], Ira D. Bloom[b], Gabriel M. Veith[a,*]

[a]Chemical Sciences Division, Oak Ridge National Laboratory, Oak Ridge, Tennessee, USA

[b]Chemical Sciences and Engineering Division, Argonne National Laboratory, Lemont, Illinois, 60439, USA

Corresponding authors: malkowskitf@ornl.gov (T. Malkowski); veithgm@ornl.gov (G. M. Veith)

Abstract

A protocol was recently developed to compare calendar life using a constant potential while monitoring the electrical current required to maintain the potential. Here, this calendar life protocol is used with electrolyte formulations containing various mole fractions of ethylene carbonate (EC), ethyl methyl carbonate (EMC), and $LiPF_6$ to elucidate the role each component plays in passivation for high silicon anodes. Together, EC and $LiPF_6$ lead to higher currents, and thus poorer passivation, whereas EMC acts as a spectator. The variation of the components' mole fraction also changes the solid-electrolyte interphase (SEI) composition, as measured by x-ray photoelectron spectroscopy. Importantly, higher $LiPF_6$ content leads to increased LiF as well as increased current, indicating that higher LiF content does not enhance the passivation of the silicon surface. Finding that EC did not yield a passivating SEI, instead ethylene sulfite, sulfolane, and propylene carbonate (PC) were used in place of EC. Using ethylene sulfite and sulfolane resulted in poorer passivation compared to EC, whereas PC resulted in superior passivation. The superior passivation may be related to more stable lithium-solvent complexes.

Keywords: silicon, lithium, anode, solid-electrolyte interphase

1. Introduction

Silicon is a potential anode material for next generation lithium-based batteries owing to its relatively low potential (<0.4 V vs. Li/Li^+) and a very high theoretical specific capacity (~3,600 mAh/g). However, several roadblocks remain for the widespread use of silicon as an anode. One particularly vexing challenge is the poor calendar life at high states of charge.[1] Composite silicon anodes show reduced cycle life and calendar life when compared to graphite, with the silicon continuing to consume electrolyte via solid-electrolyte interphase (SEI) formation and electrical isolation of active material, which suggests silicon anodes are not

effectively passivated.[1-6] Silicon passivation might be poor compared to graphite for several reasons: higher electrical conductivity or increased electron tunneling through the SEI via a thinner SEI (or shorter tunneling distance) or a lower barrier energy for electron transport; increased solvent diffusion through the SEI where it reacts at the electrode surface; or increased neutral lithium diffusion through the SEI, thereby allowing self-discharge.[7-8]

A protocol was recently developed to assess long-term electrolyte reactivity trends at the anode surface.[9] In this protocol, the cell is cycled to form the SEI and then held at a constant potential while the electrical current required to maintain the cell voltage is monitored over several hundred hours. In these tests, $LiFePO_4$ is used as a counter electrode primarily because of its flat potential profile, which reduces potential drift as the cathode is delithiated, thus maintaining the anode potential close to the target potential. Fitting the current decay profile provides a metric with which one can estimate the extent of reduction reactions occurring at the anode/electrolyte interface; ultimately, the behavior can be correlated with the calendar life achieved with the system. This protocol helps separate instances of SEI chemical instability (i.e. the SEI dissolves away or is permeable to some reacting species) from SEI that is unstable due to the large volumetric changes from lithiation/delithiation.[2] By maintaining a constant potential at the electrodes, the lithium content of the electrodes remains (nearly) constant, thus removing any mechanical strain or cracking that would normally result from lithiation/delithiation.

In this work, we used the above calendar life evaluation protocol to understand the role of the electrolyte components in the formation of a SEI. Classic reaction kinetics measurements estimate rate constants and mechanisms of chemical reactions by monitoring the concentration of products or reactants through many methods, including ultraviolet/visible light absorption, infrared spectroscopy, NMR, and mass spectrometry.[10-12] By varying the ratio (and thus the activity) of reagents, one can estimate the reaction orders and the mechanistic importance of various constituents. Although many of the spectroscopic methods mentioned above cannot be applied easily to assembled electrochemical devices, current techniques provide a direct measure of electron transfer rates. We varied the ratios of constituents in the electrolyte and monitored the current required to maintain a constant voltage (henceforth referred to as the *residual current*) as a measure of the parasitic reactions occurring within the SEI to explore which electrolyte species is responsible for the SEI's non-passivating behavior.

A general electrochemical reaction might proceed as $A + e^- \rightarrow B^-$, where A is some reactant and B^- is the product. Because every A converted to B^- consumes an electron, the current flowing to the reaction zone can be used as a measure of the reaction rate. However, the flowing current will ultimately be the sum of any electrochemical reactions occurring in parallel as well as the electronic current (current caused by the finite electronic conductivity of the medium). Although the identity of the product is lost, measurement

of the current over time at a constant voltage will yield the total reaction rate, and its integral will yield the total reacted charge, assuming the electronic current through the electrolyte is negligible. Using this method, the $LiPF_6$ + ethyl methyl carbonate (EMC) + co-solvent (ethylene carbonate [EC], propylene carbonate [PC], ethylene sulfite [ES], or sulfolane) electrolyte system with a lithium iron phosphate (LFP) cathode and silicon anode was studied in a full cell configuration. By fitting the decay rate of the residual current, we were able to extract phenomenological information, identify the unstable chemical components, and correlate them to the passivating power of the SEI.

2. Experimental

The LFP cathodes and silicon anodes were fabricated at Argonne National Laboratory's (Argonne's) Cell Analysis, Modeling, and Prototyping (CAMP) facility. The cathode was made from LFP (Johnson Matthey, 90 wt %) with 5 wt % PVDF and 5 wt % C45 carbon black. The anode was made from 80 wt % silicon (Paraclete Energy Inc., milled silicon), 10 wt % C45 carbon black and 10 wt % LiPAA (85% neutralized). The cast cathode and anode materials were dried under vacuum overnight (>12 hours) at 120°C and 150°C, respectively, and were subsequently transferred to an argon-filled glovebox while still hot. Importantly, the areal loading of the LFP (>4 mAh/cm^2) was much larger than that of the anode (~1.2 mAh/cm^2 when lithiated to 100 mV vs. Li/Li^+) to guarantee that the quasi-constant potential of the cathode was maintained during the voltage hold experiment despite the low initial coulombic efficiency of the silicon electrode.[9] Electrolyte solutions were made in an argon-filled glovebox by weighing out the proper amount of solvent (EC, Sigma-Aldrich 99%), PC (Sigma-Aldrich 99.7%), ES (Sigma-Aldrich ≥99.0%), sulfolane (Sigma-Aldrich 99%), and diluent. In all cases, the diluent was EMC (Sigma Aldrich, 98%). The solvent and diluent were then mixed and dried over zeolites (3A) and lithium metal. The lithium metal was reacted, and then replaced with new lithium until the lithium had been shiny for >24 hours. Subsequently, 4 mL of EC/EMC was measured out with a micropipette and the proper amount of $LiPF_6$ was weighed out and added to form the final electrolyte solution. Celgard 2325 separators were then soaked in the electrolyte solution for a minimum of 24 hours to ensure wetting before cell assembly.

Coin cells (CR2032, stainless steel parts with polypropylene gasket) were assembled in an argon-filled glovebox. The LFP had an areal capacity of ~4.02 mAh/cm^2, whereas the silicon had an areal loading capacity of 3.96 mAh/cm^2. The LFP was 15 mm in diameter, the silicon was 14 mm in diameter, and the separator was 19 mm in diameter. Coin cell parts were first cleaned in an ultrasonic bath of hexane and then isopropanol for 15 minutes each before drying overnight at 105°C. The parts were then transferred into the glovebox while still hot. The coin cells were assembled by first placing a spring and spacer into the coin cell bottom. The cathode was then placed on the spacer, and 50 µL of electrolyte was placed on top of the cathode. A separator soaked in electrolyte was then placed on the cathode, and an additional 50 µL of

electrolyte was placed on top of the separator. The anode was then placed in such way that the electrolyte wetted active material, and the cell was sealed. The cell was then removed from the glovebox and connected to a Maccor 4000 cell tester. Each cell was cycled 3 times from 2.7 to 3.35 V at C/10 and then charged up to 3.35 V and held while the current was measured. Cell capacities were approximately 3 mAh and were run in triplicate to ensure reproducibility.

Electrolyte conductivity was measured using a Swagelok® cell design with glassy carbon electrodes (CH Instruments, CH104). The cell was first assembled without the electrolyte to set the ferrules in place on the electrodes (to ensure the same distance is set each time the cell is assembled). The cells were initially cleaned via rinsing with deionized water and isopropanol. The cells were then dried overnight at 80°C under vacuum and then placed in an argon-filled glovebox. The electrolyte was loaded into the cells, and the cells were sealed. Impedance spectra were taken using a Bio-Logic SP240 potentiostat in potentiostatic mode with a 10 mV signal amplitude and current ranges of 100 μA, 1 mA, and 10 mA. The cells were cleaned with isopropanol and allowed to air dry between electrolytes. Subsequently, a 0.01 N aqueous potassium chloride solution was used as a conductivity standard (σ_{KCl} = 1.41 mS/cm) for each cell, and the measured conductivity of each electrolyte was determined by the following equation: $\sigma_{electrolyte} = \sigma_{KCl}\frac{R_{electrolyte}}{R_{KCl}}$.

After cycling, x-ray photoelectron spectroscopy (XPS) was performed on the anode surface. Working in an argon-atmosphere glovebox, the cells were disassembled, and the electrodes were retrieved. Samples were taken from the negative electrodes and cleaned by swirling twice in an excess dimethyl carbonate solution for 1 minute. The rinsed electrode samples were analyzed in an XPS system (Physical Electronics PHI 5000 VersaProbe II) under a high vacuum and typical pressures below 5×10^{-8} Torr. Because this system was attached to the glovebox, samples could be inserted into the XPS analysis chamber without exposure to ambient air. The sample analysis area was 100 μm^2. For this analysis, an aluminum Kα x-ray monochromator (hν = 1486.6 eV) operating with an anode power of 25 W was used. A charge neutralizer compensated for any sample charging. Other conditions included the following: the sample surface was normal oriented at 45° to the x-ray source and photoelectron spectrometer, the spectrometer pass energy was set to 23.5 eV for high-resolution spectra collection, and spectra calibration was done with the C-C peak at 284.8 eV. For all XPS spectra, the Multipack software from Physical Electronics was used to perform Shirley background subtraction and curve fitting to multiple Gaussian peaks. The estimated uncertainty in the atomic concentrations in the spectra was ~10%.

3. Data Reduction

Cell capacity data were measured via the formation cycles from 2.7 to 3.35 V. The data from the voltage-hold period were normalized to the total charge capacity immediately before the hold (i.e., the charge

capacity of the last formation cycle) to correct for cell-to-cell variation. Both the constant-current and constant-voltage capacity values were included in the total charge capacity value. Complex kinetic interactions will dominate the current behavior initially, which makes developing a reasonable model intractable that early in the test. Thus, we chose to analyze the data under the assumption of diffusion-limited growth, which would only be valid as equilibrium is approached. The justification for the mathematical model, in which the current-limiting mechanism is diffusion through the SEI, is illustrated in Figure 1. The SEI is assumed to increase in thickness linearly with the charge passed through it, thus leading to a $t^{1/2}$ dependence. To meet the requirement of a diffusion-limited growth regime, the data for the fitting exercise started at t = 80 hours and ended at the termination of the aging period.

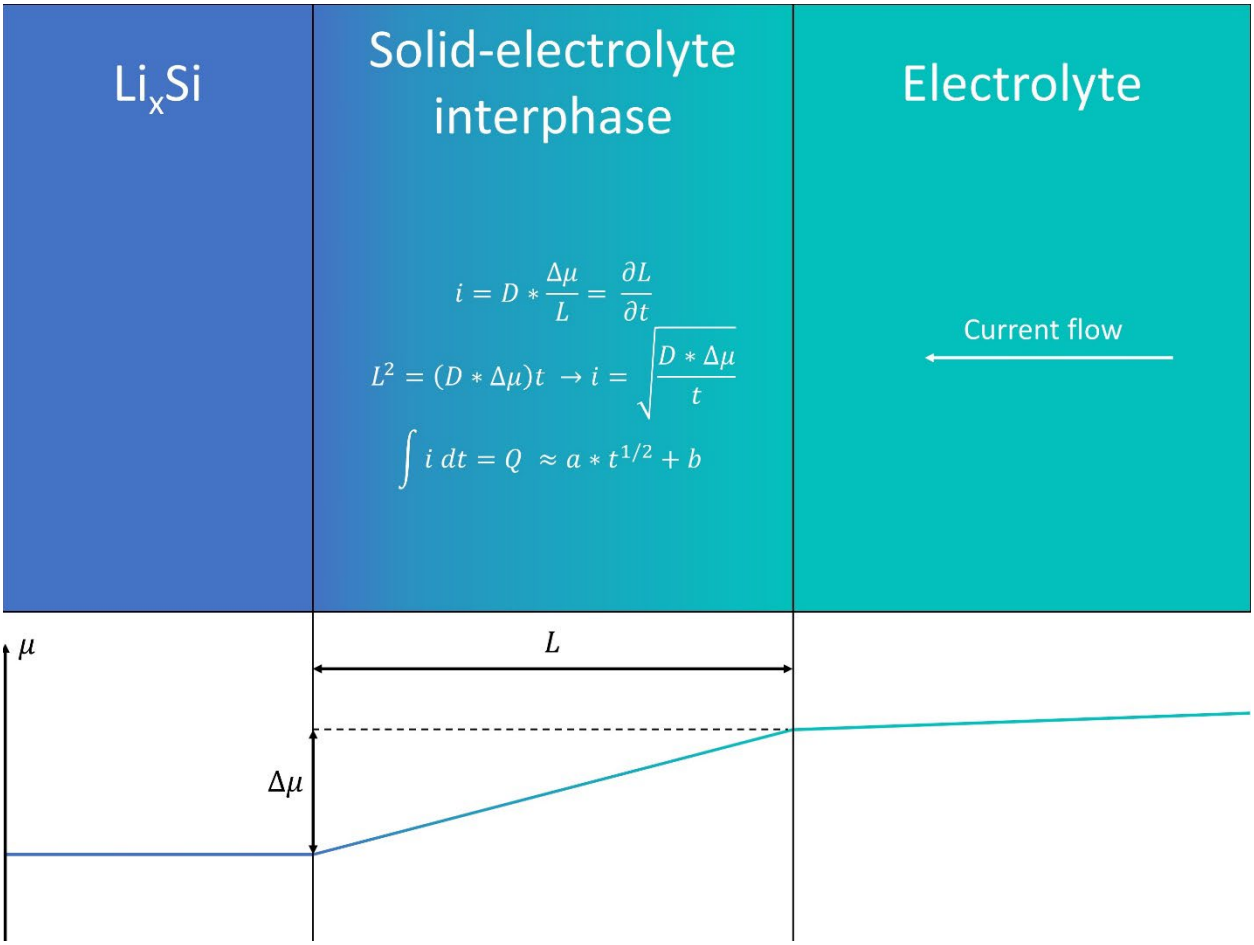

Figure 1. Schematic of model used to fit the total charge (integration of residual current), where i is the current, μ is the chemical potential of lithium, D is the diffusivity of lithium, and Q is the total charge passed. The bottom shows the variation of the lithium chemical potential across the boundary between the silicon anode (left) and the bulk electrolyte (right). The current across the SEI (middle) is assumed to be diffusion limited and thus would have a linear gradient across the SEI.

The normalized capacity, $\hat{Q} = at^{1/2} + b$, was fit using robust regression methods. Tukey's biweight function, with a tuning constant of 6, was used to iteratively reweight the data, thereby minimizing the

effect of data scatter on the fit.[13-16] The regression coefficient, r^2, was calculated using Eq. 1, where *TSS* is the total sum of squares, Q is the experimental observation, $\hat{Q}$ is the estimate from the fit, $\bar{Q}$ is the arithmetic average of the values, and *RSS* is the residual sum of squares. The fitting process was implemented in a Visual Basic for Applications (VBA) macro in Microsoft Excel.

$$TSS = \sum(\bar{Q} - Q)^2$$

$$RSS = \sum(\hat{Q} - Q)^2 \qquad (1)$$

$$r^2 = \frac{TSS - RSS}{TSS}$$

The two most similar values of a (and the corresponding values of b) were then correlated with the electrolyte composition using Scheffé's statistics-of-mixtures methods.[17-18] The complete, 10-term equation for a 3-component system is given in Eq. 2 for $\hat{a}$ and $\hat{b}$. Here, x_1 was the mole fraction of EC; x_2, the mole fraction of EMC; and x_3, the mole fraction of $LiPF_6$ in the bulk electrolyte. Eq. 2 assumes that $x_1 + x_2 + x_3 = 1$. The coefficients from the fit are α_n and A_n for $\hat{a}$ and β_n and B_n for $\hat{b}$.

$$\begin{aligned}\hat{a} = {} & \alpha_1 x_1 + \alpha_2 x_2 + \alpha_3 x_3 + \alpha_{12} x_1 x_2 + \alpha_{13} x_1 x_3 + \alpha_{23} x_2 x_3 + A_{12} x_1 x_2 (x_1 - x_2) \\ & + A_{13} x_1 x_3 (x_1 - x_3) + A_{23} x_2 x_3 (x_2 - x_3) + \alpha_{123} x_1 x_2 x_3\end{aligned} \qquad (2)$$

$$\begin{aligned}\hat{b} = {} & \beta_1 x_1 + \beta_2 x_2 + \beta_3 x_3 + \beta_{12} x_1 x_2 + \beta_{13} x_1 x_3 + \beta_{23} x_2 x_3 + B_{12} x_1 x_2 (x_1 - x_2) \\ & + B_{13} x_1 x_3 (x_1 - x_3) + B_{23} x_2 x_3 (x_2 - x_3) + \beta_{123} x_1 x_2 x_3\end{aligned}$$

A VBA macro was written in Microsoft Excel to use robust regression to search for all combinations of terms that would meet the following criteria: the value of r^2 was ≥0.95; the fewest number of fitting terms were used so that the fit was overdetermined; and most of the fitting parameters satisfied Eq. 3. The last criterion ensured that the value of the fitting parameter was significantly different from zero at the 95% confidence level.

$$\frac{uncertainty\ in\ a\ parameter}{|\ value\ of\ the\ parameter|} < 0.5 \qquad (3)$$

The uncertainty in each fitting coefficient was computed as follows. The mean square residual (M) was calculated from $M = RSS/n$, where n is the number of observations. The experimental x-values were arranged as the columns of a matrix, $\boldsymbol{D}$, and Eq. 4 was used:

$$\boldsymbol{V} = ((\boldsymbol{D}^{\mathrm{T}}\boldsymbol{w})(\boldsymbol{w}\boldsymbol{D}))^{-1} \qquad (4)$$

where $\boldsymbol{w}$ is the weight matrix from the robust regression. The uncertainties, U_k, were calculated from Eq. 5:

$$U_k = \sqrt{M \times V_{k,k}} \quad (5)$$

where $V_{k,k}$ are the values on the main diagonal of matrix $\boldsymbol{V}$.

The results from the selected polynomials were calculated using Microsoft Excel and plotted as contours using OriginLab Origin.

The composition data from the XPS (in atom %) was modeled using the same techniques. Here, relationships between Li<u>F</u>, $Li_xP_yO\underline{F}_z$, <u>C</u>-C, <u>C</u>=O, O-<u>C</u>=O, and <u>C</u>-O and the electrolyte compositions were found. It should be noted that the notation D-<u>E</u>-F is used to indicate the element of interest, E, in a chemical environment defined by D and, if present, F. An example of this is Li<u>F</u>, which indicates fluorine in a lithium fluoride environment.

4. Results

4.1 EC/EMC/$LiPF_6$

Using the principles from kinetic analysis of reactions, a variety of electrolyte mixtures were prepared to form a composition matrix. A composition map of the various tested electrolytes is shown in Figure 2. A range of electrolyte compositions was chosen to allow the deconvolution of the impact of the various electrolyte components. The concentration of $LiPF_6$, EC, and EMC were varied to determine the effect of each component on parasitic reactions. In the ideal case, the electrolyte components would not interact, and the leakage current, *i*, could be expressed as a sum of individual reactions, $i = k_{EC}[EC]^{\alpha} + k_{EMC}[EMC]^{\beta} + k_{LiPF_6}[LiPF_6]^{\gamma}$, where k_x is the reaction rate constant for component x. However, in an operating cell, the components may interact, thereby yielding cross-product terms (e.g., $k_{EC-LiPF6}[EC]^{\alpha_1}[LiPF_6]^{\gamma_1}$). As will be discussed, this was indeed the case, and a more sophisticated analysis method was required to deconvolute the results into individual components.

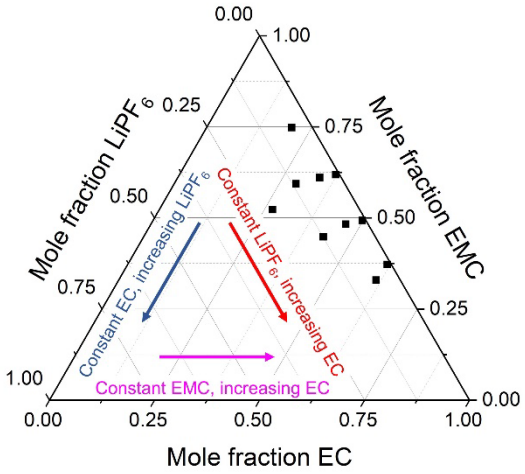

Figure 2. Composition map of various electrolyte compositions in mole fraction. Lines parallel to the EMC axis indicate constant $LiPF_6$ mole fraction, lines parallel to the $LiPF_6$ axis are constant EC mole fraction, and lines parallel to the EC axis are constant EMC mole fraction.

Figure 3. For all electrolytes, the residual current started at the charging rate (0.3 mA) and decayed by ~2 orders of magnitude within the first 200 hours at the potential hold. For higher $LiPF_6$ concentrations, the decay rate was slower, leading to higher currents at shorter timescales. For example, for an EMC mole fraction of 0.62, the electrolyte with 0.01 mole fraction $LiPF_6$ had currents 41%, 46%, and 31% smaller than the electrolyte with 0.05 mole fraction $LiPF_6$ at 50, 100, and 500 hours.

The residual current increased with increasing EC mole fraction for all $LiPF_6$ concentrations. For the majority of $LiPF_6$ concentrations (except for 0.01 mole fraction $LiPF_6$), the residual current at long times (>400 hours) remains higher with higher EC concentration. However, at 0.01 mole fraction $LiPF_6$, the currents converge to a similar value. As the $LiPF_6$ concentration increases, the residual current also increases, which indicates that both EC and $LiPF_6$ contribute to the residual current. Very high concentrations of $LiPF_6$ give rise to unsteady current decay (see Figure 3c), which possibly indicates uneven current distribution or, more likely, precipitation.

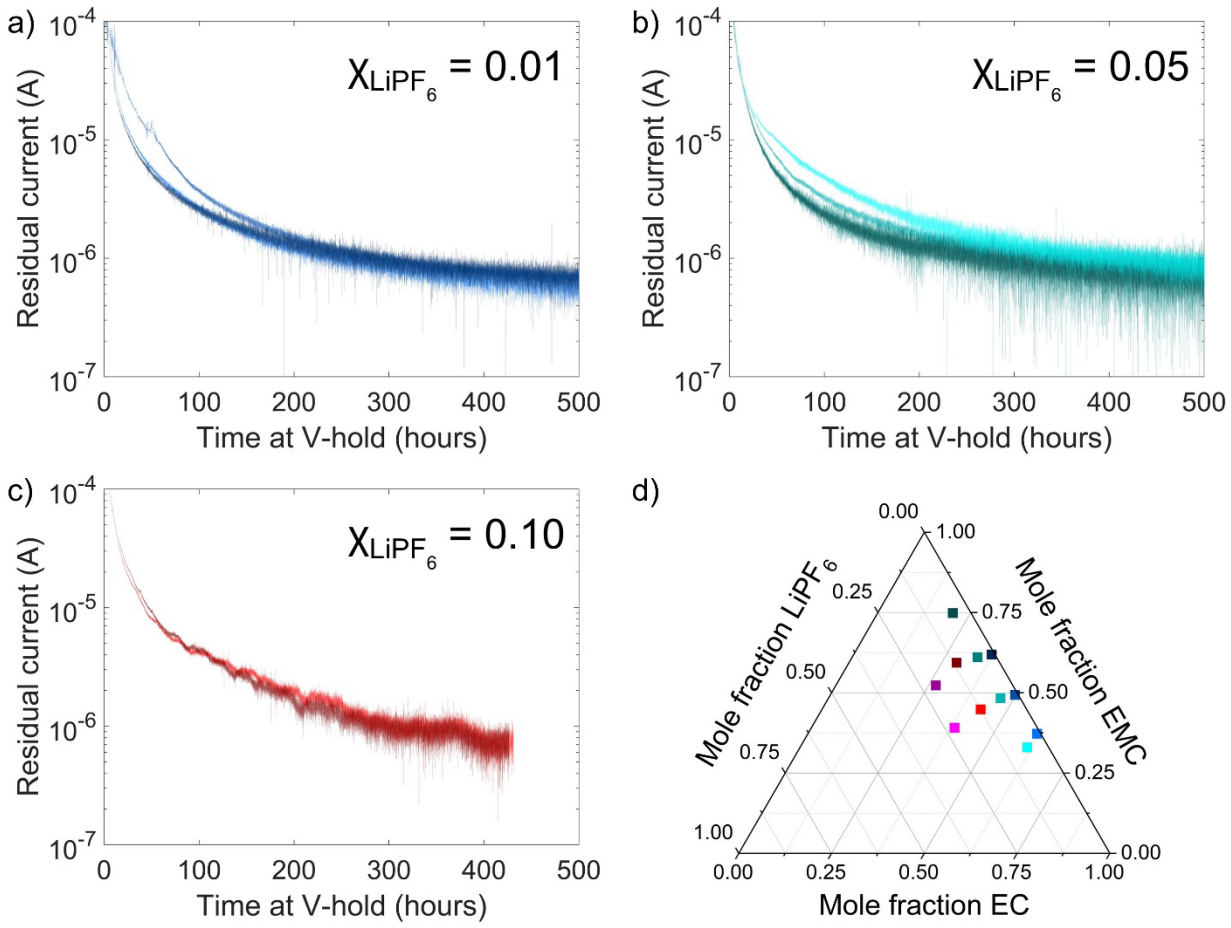

Figure 3. Time at constant voltage vs. residual current for electrolytes with $LiPF_6$ mole fraction of (a) 0.01, (b) 0.05, and (c) 0.10 and (d) the composition map for the currents shown. The composition map is of the electrolytes in the EC/EMC/$LiPF_6$ system studied here. Note that darker colors on a single plot indicate reduced EC mole fraction. The colored data points in panel (d) correspond to the electrolyte compositions of the corresponding colored currents shown in panels (a–c).

To explore this further, the integration of the residual current was also analyzed to elucidate any correlations with electrolyte components. The results from fitting $\hat{Q} = \hat{a}t^{1/2} + \hat{b}$ to the cell capacity data are shown in Table S1; the data was fit such that t = 0 corresponds to 80 hours after the start of the voltage hold, thus

t = time at voltage hold − 80 hours. The value of r^2 for all fits was 0.99 or greater, which indicates that all fits were very good.

The statistics-of-mixtures method, described in the Experimental section, was used to find relationships between the residual currents and the compositions of the electrolytes. Over 1,000 polynomials were evaluated for both $\hat{a}$ and $\hat{b}$. The selected polynomial for $\hat{a}$ was $\hat{a} = \alpha_1 x_1 + \alpha_3 x_3$. The values of α_1 and α_3 were 7.15×10^{-4} (1.69×10^{-4}) and 6.77×10^{-3} (6.95×10^{-4}), respectively, with the value in parentheses representing the uncertainty in the value. The value of r^2 was 0.95. The selected polynomial for $\hat{b}$ was more complex: it contained eight terms, $\hat{b} = \beta_1 x_1 + \beta_2 x_2 + \beta_3 x_3 + \beta_{12} x_1 x_2 + \beta_{13} x_1 x_3 + \beta_{23} x_2 x_3 + \mathrm{B}_{13} x_1 x_3 (x_1 - x_3) + \beta_{123} x_1 x_2 x_3$. The coefficients and their uncertainties for $\hat{b}$ are given Table S2.

Estimates of $\hat{a}$ and $\hat{b}$ were calculated using Eq. 4 and the values above. The results are shown in Table S1 for the electrolyte compositions used in this study. Overall, the calculated and experimental values have good agreement. The polynomial and coefficients for $\hat{a}$ indicate that EC and $LiPF_6$ contribute to $\hat{a}$. Based on the coefficients α_1 and α_3, the contribution to the residual current from $LiPF_6$ is about 10× more than the contribution from EC.

Examining the values in Table S2 shows that the linear terms, x_1, x_2, and x_3 have negative coefficients, which implies that EC, EMC, and $LiPF_6$, acting alone, tend to decrease $\hat{b}$. The three positive coefficients are in the second-order terms, x_1x_2, x_1x_3, and x_2x_3, which indicates that the pairwise interaction of EC, EMC, and $LiPF_6$ tend to increase $\hat{b}$. Indeed, the coefficients of x_1x_3 and x_2x_3 are larger than the pairwise coefficient of x_1x_2. This may indicate that much of the increase tends to come from the interaction of the organics with $LiPF_6$, with the interaction of EC with $LiPF_6$ contributing the most. This is consistent with the results discussed above.

The equation and values of the coefficients were used to calculate the estimated response in the compositional space of interest. These results are shown as contour diagrams in Figure 4. The interaction terms in the time-capacity analysis here highlight the necessity for a composition series with new electrolyte chemistries.

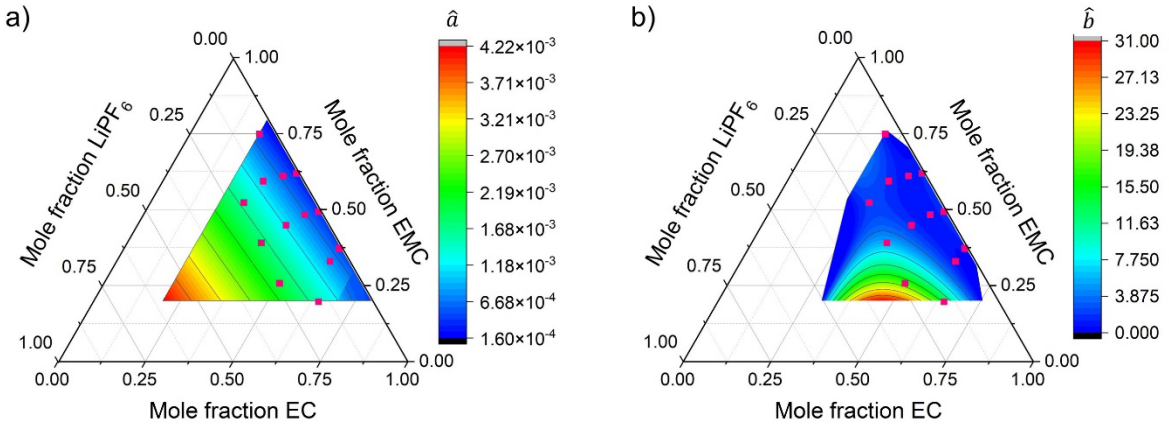

The difference in residual current behavior could be caused by changes in the SEI, thus XPS was performed to investigate further. The primary SEI components observed were Li_2CO_3, LiF, $Li_xPO_yF_z$, carboxylate groups, alkoxide groups, and alkane groups. Contour maps of the SEI components are shown in Figure 5. All SEI components showed a dependence on the electrolyte composition, which indicates that the SEI can be modified by adjusting the electrolyte composition without the addition of additives. High concentrations of $LiPF_6$ and EC lead to increased LiF in the SEI, whereas the alkane content has a minimum mole fraction between 0.6 and 0.7 EMC. At low $LiPF_6$ concentration, $Li_xPO_yF_z$ content has a local maximum at an EC:EMC ratio of 1:1; however, at much higher $LiPF_6$ concentrations, the $Li_xPO_yF_z$ content again increases. Carboxylate content tends to decrease with increasing $LiPF_6$, whereas the alkoxide content increases with higher EC content and decreases with higher $LiPF_6$ content. Li_2CO_3 was not detected in all samples but has a maximum with higher EC content, see Figure 5a. Correlating these patterns with the residual currents indicates that none of the SEI components observed can be directly connected to a reduced residual current. Higher current is observed in higher $LiPF_6$ electrolyte compositions, in which higher LiF is observed in the SEI, whereas similarly higher EC electrolyte composition leads to higher alkane content in the SEI; neither LiF nor the alkane groups show any evidence of reducing the residual current. Figure 6 shows the time vs. residual current as well as LiF (Figure 6a) and alkane (Figure 6b) composition of the SEI; the data shows that neither component suppressed the residual current. This indicates that, within the EC/EMC/$LiPF_6$ system, there is a tradeoff between conductivity (via $LiPF_6$ concentration) and stability; increasing the $LiPF_6$ content always increases the residual current. For stability, $LiPF_6$, EC, or both must be removed.

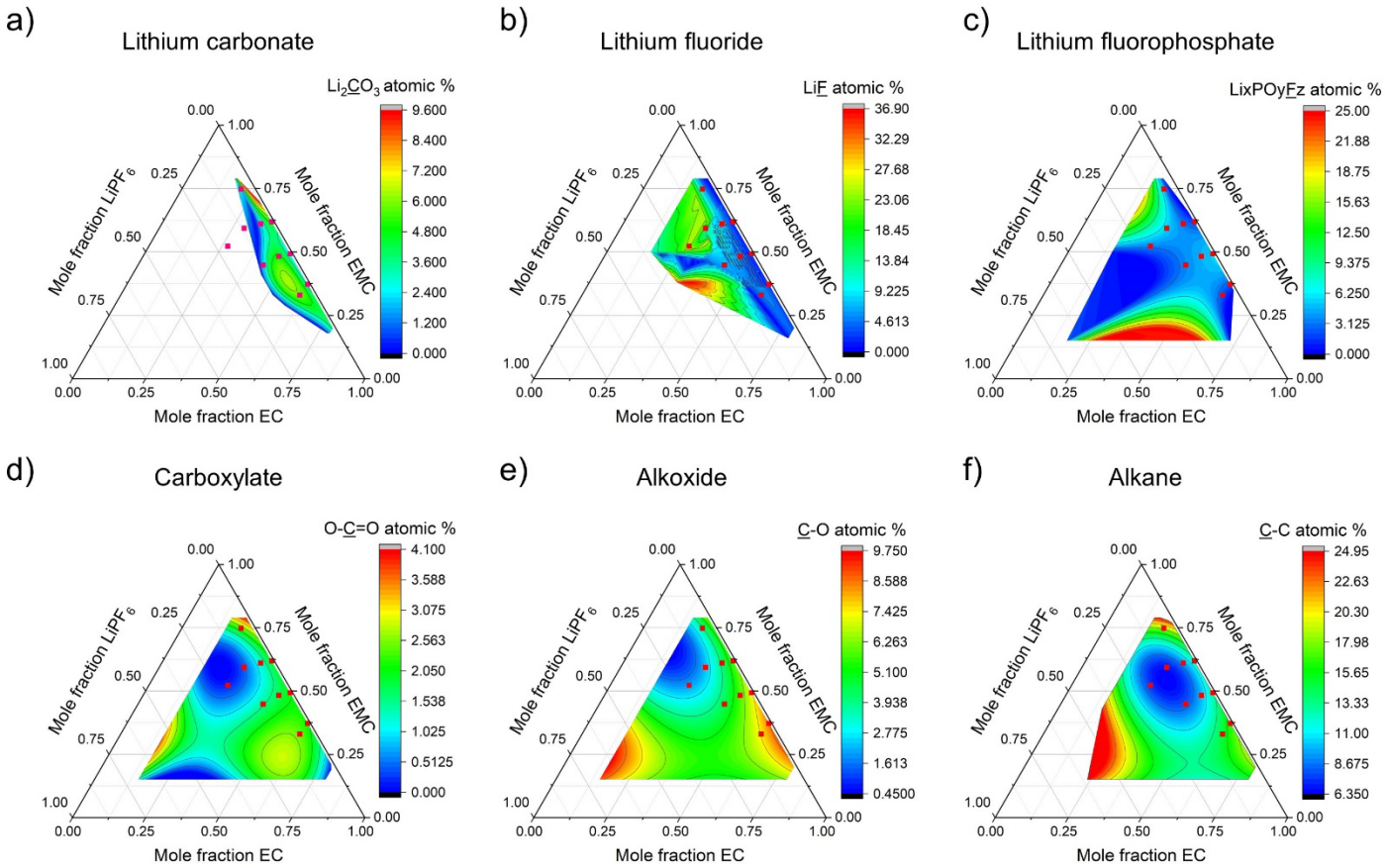

Figure 5. Contour maps of SEI composition overlayed on electrolyte composition maps. Color scales indicate the atomic % of the SEI composed of the given chemical species. Red dots indicate the compositions of the various electrolytes tested. The colormap is derived from fits to the XPS data. Note that none of the SEI components follow the same trend as the decay currents, which indicates no direct correlation between the SEI composition and the residual current.

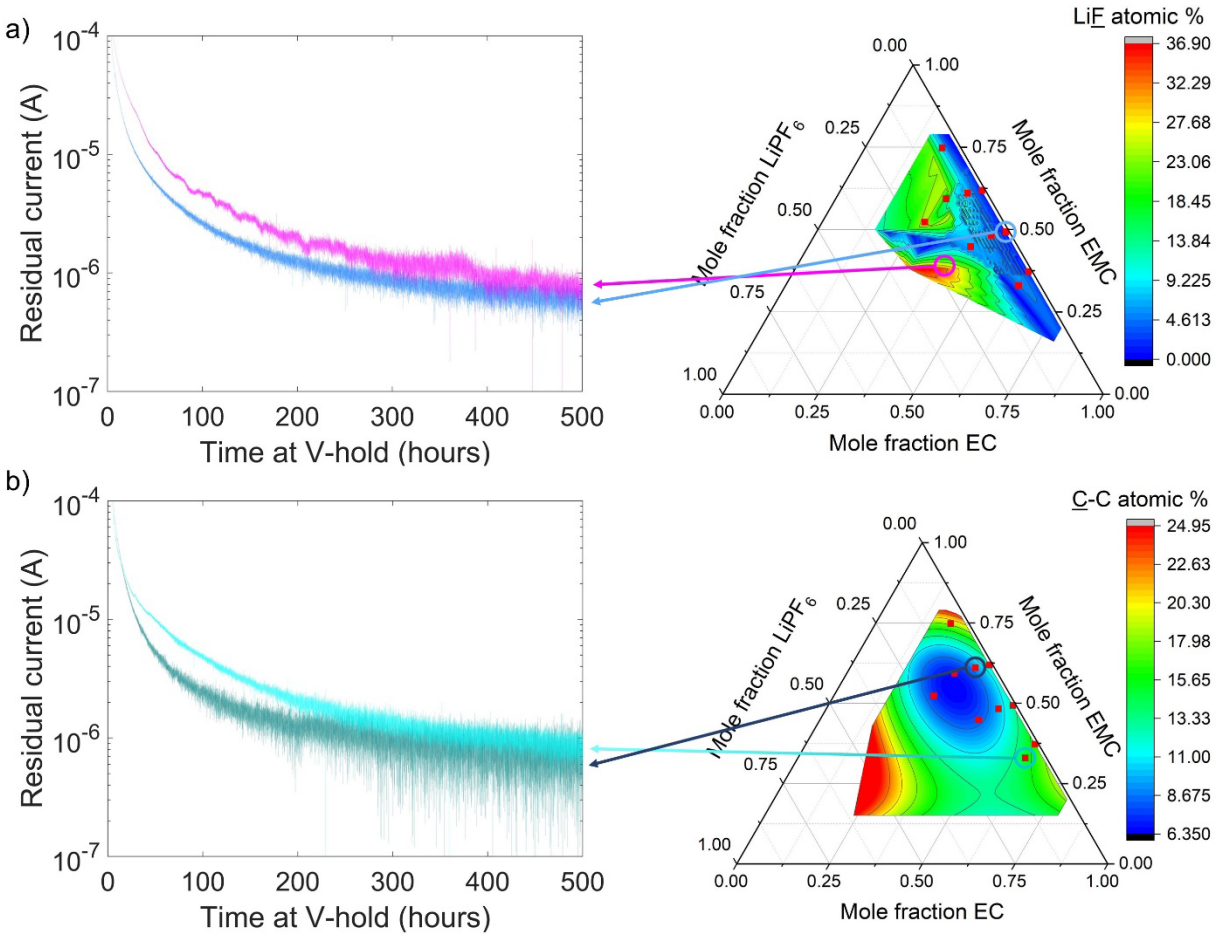

Figure 6. Comparison of time vs. residual current (left) to the electrolyte compositions (right). Note that neither LiF nor the alkane groups show any evidence of reducing the residual current.

The statistics-of-mixtures model was used to elucidate the relationship between electrolyte composition and the concentration of the chemical environments indicated in Table S3. Using the selection criteria given in the Experimental section, a polynomial fit was calculated for each chemical environment. The polynomial form and coefficients are listed in Table S4 along with the values of r^2. The complexity of the fitted polynomials indicates that the SEI composition strongly depends on the interaction between all electrolyte components. For example, the $Li_xPO_y\underline{F}_z$ content has negative coefficients for EC and high-order interactions between EC, EMC, and $LiPF_6$, which indicates that these impede the formation of $Li_xPO_y\underline{F}_z$, whereas the interaction of EC + EMC and EC + $LiPF_6$ are positive, which indicates that these interactions assist in the formation of $Li_xPO_yF_z$. The formation of $\underline{LiF}$ arises primarily from the interaction of EMC + $LiPF_6$, denoted as the $c_{23}x_2x_3$ term. A smaller amount comes from the interaction of EC and $LiPF_6$. Chemically, these results are reasonable because both LiF and $Li_xPO_yF_z$ are formed by the decomposition of $LiPF_6$. However, as mentioned before, none of the chemical environments appear to reduce the residual current, which leads one to conclude that either EC or $LiPF_6$ must be removed from the system to improve

stability. Furthermore, the formation of excess LiF does not enhance electrode passivation in the charged state.

4.2 Co-solvent/EMC/$LiPF_6$

It is clear from the residual currents in the EC/EMC/$LiPF_6$ system that, although an optimal composition may exist, the residual current still consumes too much capacity to be practical in a battery system. The variation in decay current with both $LiPF_6$ and EC suggests that replacing either component could lead to a reduction in residual current. Thus, other co-solvents (replacing EC) were explored by keeping the co-solvent:EMC mole ratio at 1:2 with 1 M $LiPF_6$. Figure 7 shows the time vs. residual current for EC, PC, ES, and sulfolane. Except for ES, all co-solvents showed a smooth decay in the residual current over time. The ES electrolyte did cycle, but the potential hold showed erratic currents that indicate the ES/EMC/$LiPF_6$ electrolyte does not passivate the silicon anode. As shown in Figure 7, the co-solvent can dramatically alter the residual current. Both sulfur-containing co-solvents (ES, sulfolane) show much higher residual currents (up to 2×) than either PC or EC. Sulfolane shows high currents of around 70 μA at 500 hours, whereas EC shows around 40 μA. Interestingly, PC shows a reduced current of ~35 μA (~12% lower than EC) at 500 hours. Clearly, the substitution of other cyclic compounds for EC significantly impacts the residual current, which proves that EC does not fully passivate silicon surfaces and suggests that other co-solvents may enhance stability.

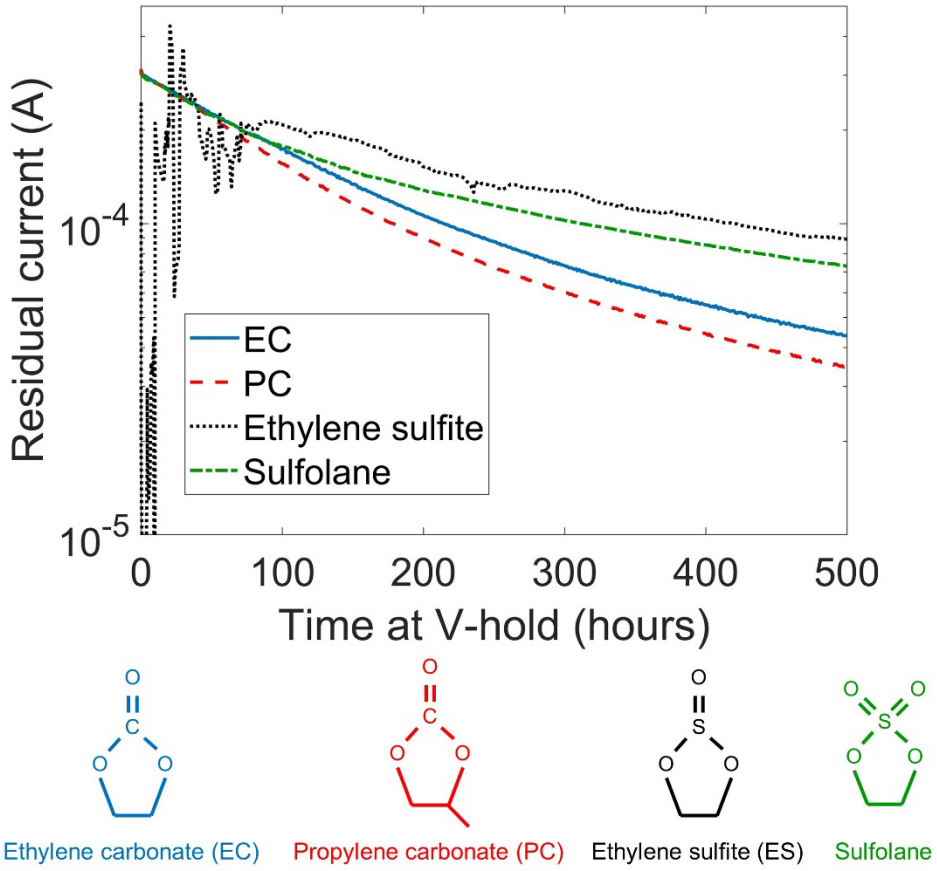

Figure 7. Time after starting potential hold vs. residual current for various co-solvents with a 1:2 co-solvent:EMC mole ratio with co-solvent structures shown below. Note that the erratic current of the ES implies the solvent is highly unstable.

The methodology employed here was used to map out the relationship between SEI stability and the electrolyte composition for silicon anodes. By design, the method accounts for interaction between components, which leads to a deeper understanding of the impact of each component on the stability of the system. For example, the analysis of the interaction between components (represented by βs in $\hat{b}$) shows strong coupling between $LiPF_6$ + EC ($\beta_{13} = 1451.34$) and $LiPF_6$ + EMC ($\beta_{23} = 801.66$), whereas EC + EMC ($\beta_{12} = 60.58$) has almost no impact. This agrees well with the contributions to $\hat{a}$, to which only $LiPF_6$ and EC contribute. Given the weak contributions of EMC to $\hat{a}$ or $\hat{b}$, the combination of EC and $LiPF_6$ appears to drive the reactions throughout the voltage hold. Klein et al. observed similar behavior while studying cells and comparing a 3:7 ratio of EC:EMC (by weight) to EMC with 1 M $LiPF_6$; they found that for high-voltage cells, the EMC cell had an SEI that was richer in $Li_xPO_yF_z$ and LiF than the EC:EMC cell.[19] If EMC equally participated in SEI formation, then the EMC cell should have similar organic content

in the SEI compared to the EC:EMC cell. Importantly, with higher $LiPF_6$ concentration, higher LiF is present in the SEI. The $LiPF_6$ concentration affected the LiF detected by XPS, as seen in Figure 5, which shows higher LiF as the $LiPF_6$ fraction increases; however, this also led to an increase in residual current. Therefore, LiF could potentially passivate the silicon surface, but its presence alone is not sufficient.[20] Similarly, an increase in the alkane groups was found in the SEI with increased EC concentration, and an increased EC concentration leads to increased residual current. Although modulation of the SEI is possible by changing the ratio of the electrolyte components, the interactions of $LiPF_6$ and EC indicate that one or both components must be removed from the system to increase stability. Given the negative correlation of $LiPF_6$ + EC with stability, it is possible that the alkane and LiF growth interfere with one another, which may result in a porous and non-passivating SEI.

Finding that both EC and $LiPF_6$ were poorly passivating and EMC was a spectator spurred the exploration of non-EC co-solvents. Replacing EC with PC is especially interesting because it led to a reduction of the residual current. Following the long-term SEI growth models suggested by Single et al., several hypotheses for the reduced residual current emerged.[7] (1) The PC SEI is more electronically insulating. In this case, the rate-limiting step of the reaction is the electron transfer to the electrolyte component that is being reduced, and a lower electronic conductivity reduces the electronic current. (2) The PC decomposition reaction's kinetics are slower than EC. In this case, there could be multiple causes, including a reduced electron transfer rate to the PC or a PC radical lifetime that is longer than the lifetime of the formed EC radical. A difference in radical lifetime could lead to alkane crosslinking, thereby decreasing pore size or changing the stability of the SEI alkane component. (3) The diffusion of reacting species that leads to self-discharge through the SEI is slower in the PC SEI than in the EC SEI. In this case, the reacting species must diffuse through the SEI, and—like in the electronic case—the diffusion through the SEI is reduced. This could be the case if solvent diffuses through the SEI to react at the anode surface or if Li^0 diffuses through the SEI to react at the SEI/electrolyte interface. (4) The coordination of PC is different from EC, and a shift in the reaction potential occurs. In this case, the PC-Li^+ complex is simply more thermodynamically stable than the EC-Li^+ complex, and thus it decomposes at a lower rate. Hypotheses 1–3 are kinetic in origin, and the reduction in current is due to a limiting rate, whereas hypothesis 4 is thermodynamic. A more insulating SEI would qualitatively explain the data because the residual current of PC is lower than the residual current for EC for essentially all times (the exception being when the potential hold begins, and the currents are the same). However, whether the PC SEI has lower electronic conductivity or reduced movement of reacting species through the SEI is not resolvable from this data. It is also possible that multiple hypotheses are true. For example, if PF_6^- is part of the solvation shell for Li^+, then the total Li^+-PF_6^--EC complex is neutrally charged and may diffuse more readily through the SEI than a charged Li^+-PC complex.

Importantly, the first 100 hours of the potential hold does not show parabolic behavior (where the current decays as $\frac{1}{\sqrt{t}}$, where t is time). Single et al. noted that for all of the models they discuss in long-term SEI growth, the time dependence is $\sqrt{t}$ for capacity (and thus $\frac{1}{\sqrt{t}}$ for current) with the exception of electron tunneling, which has a $\ln t$ dependence.[7] The long-term residual current does flatten out, which indicates a change in the current-limiting mechanism. It is impossible to know for certain based only on the residual current, but the change is likely due to a convolution of continued lithiation or self-discharge of the silicon along with electrolyte decomposition.

The stabilization of the solvated lithium complex with PC has been studied previously and supports the possibility of a more stable PC-Li^+ complex compared to an EC-Li^+ complex; computational modeling has also found PC to be more stable against reduction than EC for one- and two-electron processes.[21-22] Furthermore, our finding that the EC + $LiPF_6$ interaction drives the residual current supports a $LiPF_6$:EC complex contributing to the residual current. Using density functional theory, Xing et al. compared the inner solvation sphere energy and structure of $LiPF_6$ solvated by EC and PC. They found that although both carbonates solvate Li^+, close contact ion pairs between PF_6^- and Li^+ form more readily in EC; in other words, PF_6^- can replace an EC molecule in the inner solvation sphere, whereas it cannot replace PC.[21] Xing et al. note that the difference in the inner solvation shell may offer a different SEI, but it also implies that the PC-Li^+ complex is more stable, and thus a shift in the reaction equilibrium will be observed. This would support hypothesis 4 above (and possibly hypotheses 1 and 3, in which the SEI would be chemically altered by the presence of the PC), which indicates that at least part of the reduced residual current with PC is due to the presence of a more stable complex. If this is the case, the stabilization of the SEI may also be supported by the presence of other, more strongly coordinating solvents.

Using the dielectric constant as a metric for strength of coordination, we calculate the average dielectric constant of the solvent using $\varepsilon = \frac{\varepsilon_{co-solvent} V_{co-solvent} + \varepsilon_{EMC} V_{EMC}}{V_{co-solvent} + V_{EMC}}$, where ε_x is the dielectric constant of component x, and V_x is the molar volume of component x.[23-26] The dielectric constant vs. residual current at 150 hours of potential hold for the co-solvents/EMC series is shown in Figure 8a; for the different co-solvents, the residual current decreases almost linearly as the dielectric constant increases. It may be tempting to assume that the same convention would apply for increasing the dielectric constant by increasing the EC concentration, but Figure 8b shows a plot of the dielectric constant vs. a 150 hour residual current for a constant $LiPF_6$ mole fraction of 0.05. Although the change is much smaller in absolute current, increasing the dielectric constant almost linearly increases the residual current. When increasing the dielectric constant via changing the co-solvent, the bond strength between the coordinating solvent is increased, whereas increasing the EC concentration should not significantly change the bond strength but

will increase the average polarizability of the total medium. This suggests that highly polarizable molecules could help stabilize the lithium complexes and reduce parasitic reactions, and in the absence of known bonding energies, the dielectric strength normalized to the molar volume may act as a practical guide for complex stability.

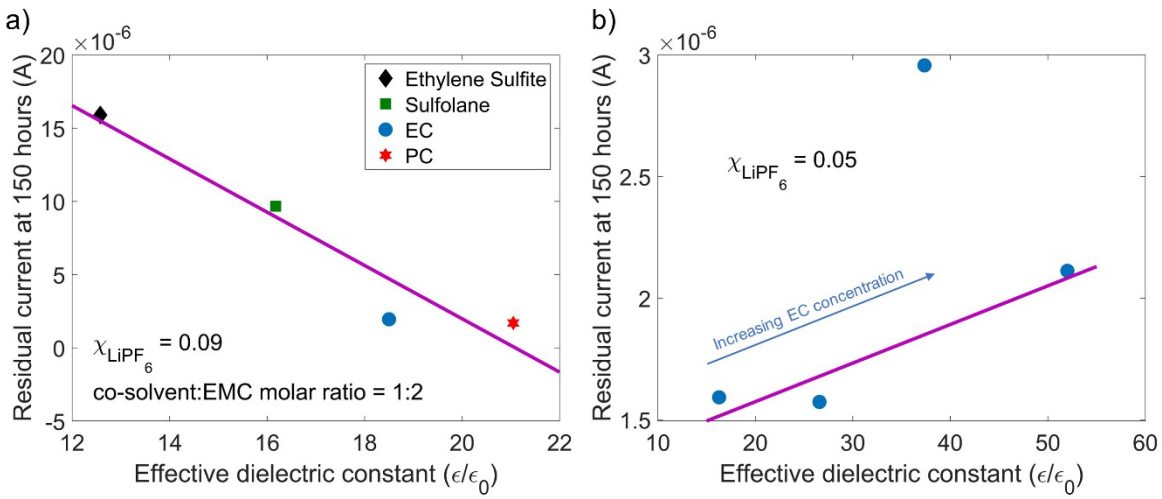

Figure 8. Dielectric constant vs. residual current after 150 hours at potential hold for (a) 1 M $LiPF_6$ ($LiPF_6$ mole fraction = 0.09) in various co-solvents/EMC and (b) constant 0.05 mole fraction $LiPF_6$ in EC/EMC. Note that the current scales are different. The lines are simply guides and do not indicate a specific quantity.

6. Conclusion

Here, we correlate electrolyte composition with the residual current from a potential hold to characterize the stability of electrolytes at the surface of silicon anodes. In this test, $LiFePO_4$ is used as a counter-electrode to maintain a constant state of charge at the anode, thereby causing the measured current to be proportional to the extent of parasitic reduction reactions at the SEI. When varying the ratios of all electrolyte components, we found that the combination of EC and $LiPF_6$ is non-passivating and contributes to higher residual current. Different co-solvents were then used in place of EC, and PC was found to reduce the residual current. The methodology used here suggests that for any new electrolyte system, a map of composition vs. electrolyte stability should be produced to determine whether a single component or the interaction of components dictates the instability of the electrolyte. This work also demonstrates that, for silicon anodes, substitution of EC can decrease the residual current, and substitution of other salts for $LiPF_6$ might lead to a similar behavior. The lack of correlation between electrolyte bulk transport properties and their ability to passivate silicon, as observed in this work, shows that optimization of electrolytes can involve nontrivial considerations for the balance of cycle and calendar lives. Given large data sets of electrolyte compositions and the resulting SEI and its passivating ability, this experimental methodology

could assist in the application of machine learning to accelerate development of next-generation electrolytes.

Acknowledgments

This research was supported by the US Department of Energy's (DOE's) Vehicle Technologies Office under the Silicon Consortium Project, directed by Brian Cunningham and managed by Anthony Burrell. This manuscript has been authored by UT-Battelle LLC under Contract No. DE-AC05-00OR22725 with DOE. Argonne is operated for the DOE Office of Science by UChicago Argonne LLC under contract number DE-AC02-06CH11357. The electrodes used in this article were made by Argonne's CAMP Facility, which was supported by the Applied Battery Research for Transportation Program directed by David Howell. The United States Government retains and the publisher, by accepting the article for publication, acknowledges that the United States Government retains a non-exclusive, paid-up, irrevocable, world-wide license to publish or reproduce the published form of this manuscript, or allow others to do so, for United States Government purposes. The DOE will provide public access to these results of federally sponsored research in accordance with the DOE Public Access Plan (http://energy.gov/downloads/doe-public-access-plan).

References

1. McBrayer, J. D.; Rodrigues, M.-T. F.; Schulze, M. C.; Abraham, D. P.; Apblett, C. A.; Bloom, I.; Carroll, G. M.; Colclasure, A. M.; Fang, C.; Harrison, K. L.; Liu, G.; Minteer, S. D.; Neale, N. R.; Veith, G. M.; Johnson, C. S.; Vaughey, J. T.; Burrell, A. K.; Cunningham, B., Calendar aging of silicon-containing batteries. *Nature Energy* **2021,** *6*, 866-872.
2. Kalaga, K.; Rodrigues, M.-T. F.; Trask, S. E.; Shkrob, I. A.; Abraham, D. P., Calendar-life versus cycle-life aging of lithium-ion cells with silicon-graphite composite electrodes. *Electrochimica Acta* **2018,** *280*, 221-228.
3. Zilberman, I.; Sturm, J.; Jossen, A., Reversible self-discharge and calendar aging of 18650 nickel-rich, silicon-graphite lithium-ion cells. *Journal of Power Sources* **2019,** *425*, 217-226.
4. Veith, G. M.; Browning, K. L.; Doucet, M.; Browning, J. F., Solid Electrolyte Interphase Architecture Determined through In Situ Neutron Scattering. *Journal of The Electrochemical Society* **2021,** *168* (6).
5. Veith, G. M.; Doucet, M.; Sacci, R. L.; Vacaliuc, B.; Baldwin, J. K.; Browning, J. F., Determination of the Solid Electrolyte Interphase Structure Grown on a Silicon Electrode Using a Fluoroethylene Carbonate Additive. *Sci Rep* **2017,** *7* (1), 6326.
6. Veith, G. M.; Doucet, M.; Baldwin, J. K.; Sacci, R. L.; Fears, T. M.; Wang, Y.; Browning, J. F., Direct Determination of Solid-Electrolyte Interphase Thickness and Composition as a Function of State of Charge on a Silicon Anode. *The Journal of Physical Chemistry C* **2015,** *119* (35), 20339-20349.
7. Single, F.; Latz, A.; Horstmann, B., Identifying the Mechanism of Continued Growth of the Solid-Electrolyte Interphase. *ChemSusChem* **2018,** *11* (12), 1950-1955.
8. Lin, Y.-X.; Liu, Z.; Leung, K.; Chen, L.-Q.; Lu, P.; Qi, Y., Connecting the irreversible capacity loss in Li-ion batteries with the electronic insulating properties of solid electrolyte interphase (SEI) components. *Journal of Power Sources* **2016,** *309*, 221-230.
9. Schulze, M.; Rodrigues, M. T. F.; McBrayer, J.; Bloom, I.; Colclasure, A.; Veith, G.; Abraham, D.; Neale, N.; Burrell, A.; Vaughey, J.; Johnson, C. *Silicon Consortium Project Calendar Aging Electrochemical Screening Protocol 1.2.*; 2021.
10. Lee, J. K.; Kim, S.; Nam, H. G.; Zare, R. N., Microdroplet fusion mass spectrometry for fast reaction kinetics. *Proc Natl Acad Sci U S A* **2015,** *112* (13), 3898-903.
11. Pintar, A.; Batista, J.; Levec, J., In situ Fourier transform infrared spectroscopy as an efficient tool for determination of reaction kinetics. *Analyst* **2002,** *127* (11), 1535-40.
12. Polster, J.; Mauser, H., Kinetic Analysis of Second Order Reactions Using UV-Vis Spectroscopy. *Talanta* **1992,** *39* (10), 1355-1359.
13. Behrens, J. T., Principles and procedures of exploratory data analysis. *Psychological Methods* **1997,** *2*, 131-160.
14. Holland, P. W.; Welsch, R. E., Robust regression using iteratively reweighted least-squares. *Communications in Statistics - Theory and Methods* **1977,** *6*, 813-827.
15. Iglewicz, B., Robust Scale Estimators and Confidence Intervals for Location. In *Understanding Robust and Exploratory Data Analysis*, Hoaglin, D. C.; Mosteller, F.; Tukey, J. W., Eds. Wiley: New York, 1983; p 417.
16. Mosteller, F.; Tukey, J. W., *Data Analysis and Regression*. 1977.
17. Scheffé, H., Experiments with Mixtures. *Journal of the Royal Statistical Society Series B - Statistical Methodology* **1958,** *20* (2).
18. Scheffé, H., The Simplex-Centroid Design for Experiments with Mixtures. *Journal of the Royal Statistical Society Series B (Methodological)* **1963,** *25* (2), 235-263.
19. Klein, S.; van Wickeren, S.; Röser, S.; Bärmann, P.; Borzutzki, K.; Heidrich, B.; Börner, M.; Winter, M.; Placke, T.; Kasnatscheew, J., Understanding the Outstanding High-Voltage Performance of NCM523||Graphite Lithium Ion Cells after Elimination of Ethylene Carbonate Solvent from Conventional Electrolyte. *Advanced Energy Materials* **2021,** *11* (14).

20. Zhao, J.; Liao, L.; Shi, F.; Lei, T.; Chen, G.; Pei, A.; Sun, J.; Yan, K.; Zhou, G.; Xie, J.; Liu, C.; Li, Y.; Liang, Z.; Bao, Z.; Cui, Y., Surface Fluorination of Reactive Battery Anode Materials for Enhanced Stability. *J Am Chem Soc* **2017,** *139* (33), 11550-11558.
21. Xing, L.; Zheng, X.; Schroeder, M.; Alvarado, J.; von Wald Cresce, A.; Xu, K.; Li, Q.; Li, W., Deciphering the Ethylene Carbonate-Propylene Carbonate Mystery in Li-Ion Batteries. *Acc Chem Res* **2018,** *51* (2), 282-289.
22. Wang, A.; Kadam, S.; Li, H.; Shi, S.; Qi, Y., Review on modeling of the anode solid electrolyte interphase (SEI) for lithium-ion batteries. *npj Computational Materials* **2018,** *4* (1), 15.
23. Chernyak, Y., Dielectric Constant, Dipole Moment, and Solubility Parameters of Some Cyclic Acid Esters. *Journal of Chemical and Engineering Data* **2006,** *51* (2), 416-418.
24. Hall, D. S.; Self, J.; Dahn, J. R., Dielectric Constants for Quantum Chemistry and Li-Ion Batteries: Solvent Blends of Ethylene Carbonate and Ethyl Methyl Carbonate. *The Journal of Physical Chemistry C* **2015,** *119* (39), 22322-22330.
25. Sears, P. G.; O'Brien, W. C., Dielectric Constants and Viscosities of Some Mono-N-Substituted Amides and Cyclic Esters. *Journal of Chemical and Engineering Data* **1968,** *13* (1).
26. Tilstam, U., Sulfolane: A Versatile Dipolar Aprotic Solvent. *Organic Process Research & Development* **2012,** *16* (7), 1273-1278.

Supplemental Information

Table S1. Values of the fitting parameters, a and b, for the electrolyte compositions

Composition (mole fraction)			Values from experimental data (uncertainty, 1-σ)		Calculated values from polynomial fit	
$LiPF_6$	EC	EMC	a, $h^{-1/2}$	b	$\hat{a}$, $h^{-1/2}$	$\hat{b}$
.009	.498	.493	5.30×10^{-4} (6.88×10^{-4})	9.37×10^{-1} (1.22×10^{-4})	4.16×10^{-4}	1.92
			9.67×10^{-4} (1.67×10^{-5})	2.03 (2.72×10^{-4})		
.010	.618	.373	6.00×10^{-4} (7.48×10^{-6})	1.06 (1.21×10^{-4})	5.08×10^{-4}	9.41×10^{-1}
			4.90×10^{-4} (6.75×10^{-6})	7.91×10^{-1} (1.10×10^{-4})		
.009	.372	.619	7.08×10^{-4} (6.93×10^{-6})	8.05×10^{-1} (1.13×10^{-4})	3.28×10^{-4}	1.35
			8.05×10^{-4} (1.17×10^{-5})	2.07 (1.91×10^{-4})		
.053	.464	.483	6.70×10^{-4} (8.30×10^{-6})	8.89×10^{-1} (1.35×10^{-4})	6.92×10^{-4}	8.08×10^{-1}
			7.87×10^{-4} (9.00×10^{-6})	1.01 (1.46×10^{-4})		
.051	.338	.611	4.95×10^{-4} (5.66×10^{-6})	7.83×10^{-1} (9.16×10^{-5})	5.89×10^{-4}	8.86×10^{-1}
			5.03×10^{-4} (5.32×10^{-6})	6.86×10^{-1} (8.62×10^{-5})		
.049	.203	.748	5.15×10^{-4} (5.64×10^{-6})	8.25×10^{-1} (9.15×10^{-5})	4.78×10^{-4}	8.25×10^{-1}
			5.31×10^{-4} (8.34×10^{-6})	9.31×10^{-1} (1.35×10^{-4})		
.058	.612	.330	6.76×10^{-4} (8.45×10^{-6})	9.47×10^{-1} (1.38×10^{-4})	7.08×10^{-4}	9.38×10^{-1}
			7.06×10^{-4} (7.01×10^{-6})	8.61×10^{-1} (1.14×10^{-4})		
.124	.428	.448	1.20×10^{-3} (2.13×10^{-5})	1.78 (3.45×10^{-4})	1.15×10^{-3}	1.78
			1.10×10^{-3} (1.80×10^{-5})	1.79 (2.92×10^{-4})		
.116	.290	.594	1.03×10^{-3} (2.05×10^{-5})	1.79 (3.34×10^{-4})	9.95×10^{-4}	1.75
			9.71×10^{-4} (1.93×10^{-5})	1.68 (3.14×10^{-4})		
.208	.270	.523	1.58×10^{-3} (2.80×10^{-5})	2.07 (4.56×10^{-4})	1.60×10^{-3}	2.13
			1.65×10^{-3} (2.59×10^{-5})	2.21 (4.22×10^{-4})		

Table S2. Values of the fitting coefficients and their uncertainties for $\hat{b}$.

Coefficient	Value (uncertainty, 1-σ)
β_1	−13.37 (6.66)
β_2	−12.18 (5.20)
β_3	−515.73 (204.60)
β_{12}	60.58 (25.17)
β_{13}	1451.34 (557.65)
β_{23}	801.66 (316.36)
B_{13}	−710.15 (275.12)
β_{123}	−1884.47 (746.43)

Table S3. Surface concentrations of observed chemical environments.

Composition (mole fraction)			LiF	C-C	C=O	O-C=O	C-O	$Li_xPO_yF_z$	Li_2CO_3
$LiPF_6$	EC	EMC							
.009	.498	.493	2.17	12.09	1.47	1.58	5.41	5.83	2.15
.010	.618	.373	1.45	17.88	2.26	2.32	9.74	2.42	3.71
.009	.372	.619	2.37	12.53	2.26	2.21	7.72	1.4	5.07
.053	.464	.483	3.99	11.04	3.69	2.22	5.44	2.94	5.78
.051	.338	.611	3.54	9.16	2.19	0.98	2.86	4.14	1.42
.049	.203	.748	7.93	18.72	2.19	2.36	4.15	4.8	2.51
.058	.612	.330	4.25	12.26	1.94	2.05	7.78	2.13	4.81
.124	.428	.448	8.68	16.12	0	1.84	3.15	3.88	2.4
.116	.290	.594	30.05	6.93	0.51	0.04	2.34	4.95	---
.208	.270	.523	29.44	7.53	0.86	0.45	3.11	3.62	---

Table S4. Polynomial coefficients for fitting functions of surface chemistry.

Chemical environment	Polynomial	Values of the respective coefficients (uncertainty, 1-σ)								r^2
$Li_xPO_y\underline{F}_z$	$c_1x_1 + c_{12}x_1x_2 + c_{13}x_1x_3 + d_{12}x_1x_2(x_1-x_2) + d_{23}x_2x_3(x_2-x_3) + c_{123}x_1x_2x_3$	−108.11 (44.71)	238.13 (93.11)	718.55 (339.00)	237.07 (97.08)	661.43 (239.91)	−1889.24 (850.83)			0.97
Li<u>F</u>	$c_3x_3 + c_{13}x_1x_3 + + c_{23}x_2x_3 + d_{23}x_2x_3(x_2-x_3) + c_{123}x_1x_2x_3$	−7417.09 (3291.37)	7715.32 (3447.23)	14782.63 (6373.21)	−7592.96 (3359.20)	−7049.55 (3338.46)				0.97
<u>C</u>-C	$c_2x_2 + c_{12}x_1x_2 + d_{12}x_1x_2(x_1-x_2) + d_{23}x_2x_3(x_2-x_3)$	84.22 (27.88)	−114.32 (55.80)	210.89 (93.47)	−374.03 (160.14)					0.96
<u>C</u>=O	$c_2x_2 + c_3x_3 + c_{12}x_1x_2 + c_{23}x_2x_3 + d_{12}x_1x_2(x_1-x_2) + d_{13}x_1x_3(x_1-x_3) + d_{23}x_2x_3(x_2-x_3) + c_{123}x_1x_2x_3$	66.29 (23.79)	−1699.43 (550.76)	−131.56 (50.53)	3640.92 (1161.73)	126.07 (49.33)	1221.02 (385.22)	−3219.76 (1052.28)	1800.49 (751.10)	0.98
O-<u>C</u>=O	$c_1x_1 + c_2x_2 + d_{12}x_1x_2(x_1-x_2) + d_{13}x_1x_3(x_1-x_3) + d_{23}x_2x_3(x_2-x_3)$	−10.85 (4.74)	14.99 (4.65)	54.24 (21.88)	75.96 (37.31)	−88.71 (23.15)				0.97
<u>C</u>-O	$c_2x_2 + d_{12}x_1x_2(x_1-x_2) + d_{23}x_2x_3(x_2-x_3)$	15.11 (1.64)	54.46 (12.25)	−114.64 (48.62)						0.96
$Li_2\underline{C}O_3$	$c_2x_2 + c_3x_3 + c_{12}x_1x_2 + d_{12}x_1x_2(x_1-x_2) + d_{23}x_2x_3(x_2-x_3) + c_{123}x_1x_2x_3$	72.41 (29.96)	−514.65 (246.953)	−138.89 (64.03)	128.72 (56.93)	−686.92 (320.07)	3071.89 (1376.72)			0.98

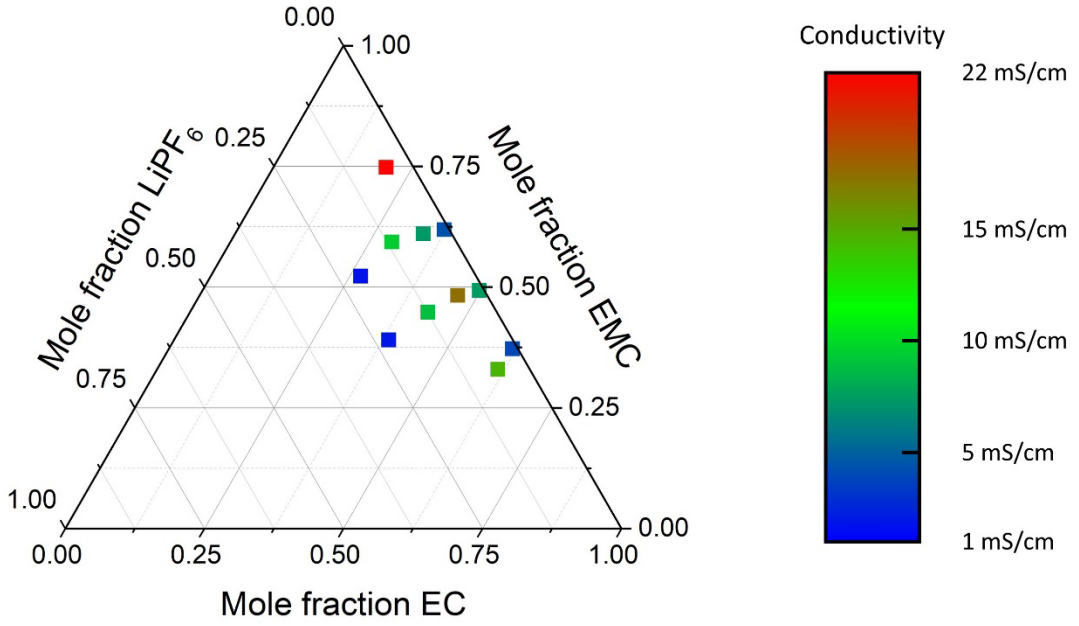

Figure S1. Composition vs. conductivity of the tested EC/EMC/$LiPF_6$ electrolytes. Note that decay current increases with increasing $LiPF_6$ and EC content, but conductivity has no such correlation. The lack of a correlation between either higher or lower conductivity with residual current shows that conductivity is not the cause of the differences in electrolyte behavior.